ISSN 0021-3640, JETP Letters, 2024, Vol. 119, No. 9, pp. 672–680. © The Author(s), 2024. This article is an open access publication.
Russian Text © The Author(s), 2024, published in Pis'ma v Zhurnal Eksperimental'noi i Teoreticheskoi Fiziki, 2024, Vol. 119, No. 9, pp. 658–667.

OPTICS
AND LASER PHYSICS

Stability of the Formation of an Image Using a Terajet with Respect to the Beam Shift

A. G. Paddubskaya[a,*] (ORCID: 0000-0001-7658-1436), A. V. Novitsky[b] (ORCID: 0000-0001-9553-7318), O. V. Minin[c,d] (ORCID: 0000-0002-9749-2106), and I. V. Minin[c,d,e] (ORCID: 0000-0002-6108-8419)

[a] *Institute for Nuclear Problems, Belarusian State University, Minsk, 220006 Belarus*
[b] *Belarusian State University, Minsk, 220030 Belarus*
[c] *National Research Tomsk Polytechnic University, Tomsk, 634050 Russia*
[d] *Siberian State University of Geosystems and Technologies, Novosibirsk, 630108 Russia*
[e] *Novosibirsk Branch of Rzhanov Institute of Semiconductor Physics SBRAS "Technological Design Institute of Applied Microelectronics," Russian Academy of Sciences, Novosibirsk, 630108 Russia*
**e-mail: paddubskaya@gmail.com*

Received March 31, 2024; revised April 9, 2024; accepted April 9, 2024

The shift of an image of a dielectric sphere asymmetrically irradiated by a terahertz Gaussian beam in terahertz imaging systems has been demonstrated experimentally. Numerical calculations using the operator scattering theory have shown the bending of the localization region of the electromagnetic field near the shadow surface of the dielectric sphere when it is shifted with respect to the waist center of the Gaussian beam, leading to the formation of the so-called "photonic hook" with the properties depending on the polarization and frequency of the incident radiation. The possibility of reaching a spatial resolution of 0.38λ in the studied range has been shown experimentally. The obtained results can be used to increase the resolution of commercial scanning terahertz systems.

DOI: 10.1134/S0021364024600939

INTRODUCTION

Significant progress has been achieved in the recent two decades in the utilization and incorporation of the terahetz frequency range of 0.1–10-THz (wavelength λ from 3 to 30 mm). In particular, terahertz radiation, which was first obtained experimentally in the 1920s [1], is widely applied in medicine, nondestructive testing, safety systems [2], and the development of 5G and 6G communication and high-speed data transmission tools [3–5]. Due to a low photon energy (1 THz corresponds to an energy of about 4 meV), terahertz waves demonstrate nonionizing interactions with matter, freely pass through nonpolar dielectrics, and are strongly absorbed by metals and polar dielectrics [6]. Furthermore, low-energy resonances of many complex organic molecules, as well as vibrational and rotational spectra of polymers, are in the terahertz range [7–9], which opens wide prospects for the further development of remote scanning, imaging, and spectroscopy technologies [10].

The spatial resolution of most of the modern terahertz scanning systems is limited by the diffraction limit depending both on the working wavelength and on the overall implementation of the system. In practice, the generated terahertz radiation is usually focused on a sample using polymeric convex lenses or off-axis metal-coated parabolic mirrors [11]. The latter are particularly interesting because they introduce minimal losses, and the off-axis geometry ensures the maximum possible focal length and the absence of ambient illumination [12]. However, it is noteworthy that the numerical aperture (NA) of the standard optical systems is usually less than 0.5 [6, 13]. As a result, the spatial resolution of such optical systems is comparable with the wavelength λ, which is 300 μm at a frequency of 1 THz, and thereby restricts their capabilities for the analyzing of objects with small transverse dimensions and spatially inhomogeneous materials.

As shown in [14–17], one of the efficient approaches to significantly increase the spatial resolution of existing terahertz systems is the localization of the electromagnetic field near the surface of the sample due to the interaction of the incident radiation with dielectric objects having dimensions from 2λ to 20λ. Diffraction on such dielectric particles results in the formation of extended regions of a high intensity, known as "photonic jets" in optics or "terajets" in the terahertz range, near the shadow surface of these dielectric particles [18]. In particular, the authors of [19–21] showed that the minimum width of the beam in the waist region of the photonic jet for dissipationless mesoparticles (sometimes called the "superlens")

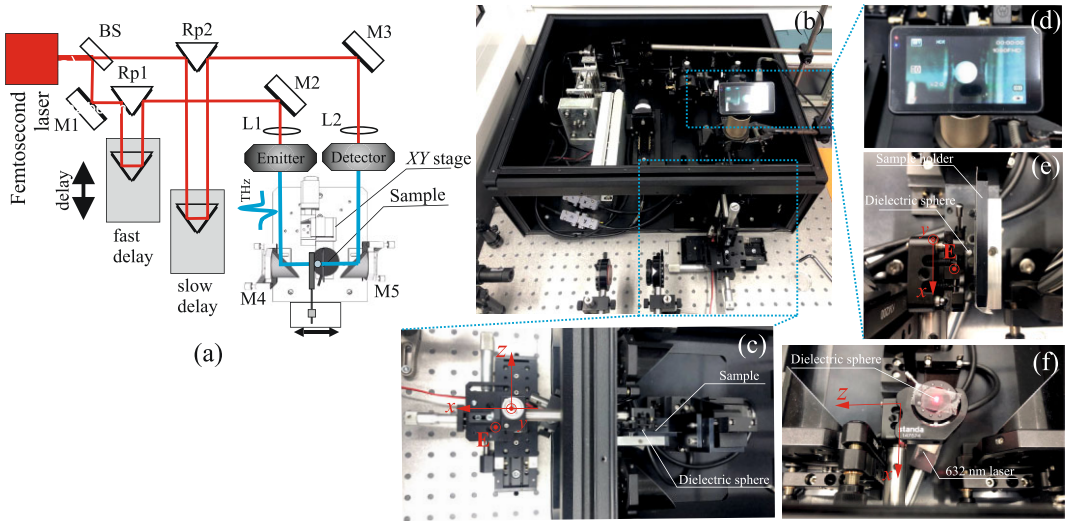

Fig. 1. (Color online) (a, b) Optical scheme and the top view of the time-resolved terahertz spectrometer T-Spec (EKSPLA, Vilnius, Lithuania). (c) Image of the three-coordinate linear translator used for the precise positioning of the dielectric sphere relative to the terahertz beam and the sample surface. (d) Magnified image of the camera monitor used to visually monitor the sphere position with respect to the sample. (e, f) Iris diaphragm with the dielectric sphere in the center.

can reach ~λ/3, which significantly higher than the spatial resolution of "classical" diffraction-limited terahertz systems.

It is worth noting that the parameters of both the photonic jet and terajet are sensitive to the dimensions and shape of a particle, its structural composition, dielectric properties, and the properties of the environment [22, 23]. In [24], we experimentally demonstrated for the first time the correlation between the terahertz spectrum transmitted through the dielectric sphere and the quality of images obtained at different frequencies. In particular, considering the scattering of the terahertz Gaussian beam on a Teflon sphere with the diameter comparable to the waist radius, we showed that images with the maximum contrast are observed near the minimum in the sphere transmission spectrum. In this context, the effect of shifting of the dielectric sphere from the center of the terahertz beam on the quality of recorded images becomes practically important. To the best of our knowledge, this effect has not yet been studied. In this work, we fill this gap by analyzing the effect of the breaking of the axial symmetry of the system with respect to the axis of the spherical superlens on the quality and structure of the recorded terahertz images.

EXPERIMENT

The scheme of the experimental setup, based on a T-Spec time-resolved terahertz spectrometer (EKSPLA, Vilnius, Lithuania), is shown in Fig. 1a. A femtosecond laser generating optical pulses with a wavelength of 1064 nm, a duration of 145 fs, and an output power of 85 mJ was used as a source of optical radiation. The main pulse of the linearly polarized laser radiation was separated by a beam splitter BS1 into two beams (55:45). The first beam was used to generate the terahertz radiation (lens L1 focused the incident beam on an emitter), while the second beam was used to detect the amplitude and phase of the transmitted signal (lens L2 focused the pump radiation on a detector). The system included fast and slow delay lines. The fast line allowed us to collect data in real time at a rate of about ten spectra per second. The additional slow delay line expands the scanning window from 110 to 220 ps. Photoconductive antennas based on low-temperature grown GaAs semiconductor structures served as the emitter and detector of terahertz waves. The generated linearly polarized terahertz radiation with the electromagnetic field distribution in the cross section well approximated by a Gaussian allows scanning in the frequency range of 0.1–1 THz.

Subpicosecond terahertz pulses were focused on the sample by two off-axis parabolic mirrors M4 and M5. To move the sample in the (x, y) plane perpendicular to the optical axis of the incident beam and to record the time spectrum at each point (mapping of the sample), the system involved two crossed motorized translation stages (see Fig. 1a), which were controlled by specially developed software. To improve the signal-to-noise ratio, additional averaging over eight measurements was performed at each scanning point. A signal was transformed from the time to the frequency domain using fast Fourier transform algorithms. The transmission spectrum detected in the experiment is treated as the ratio of the signal intensity

with the sample to the signal intensity without the sample.

The aperture of the terahertz beam in the focal plane of parabolic mirrors M4 and M5 was estimated using a method described in detail in [25]. In particular, the analysis of the transmitted signal intensity as a function of the position of a thin metallic diaphragm with respect to the center of the beam and its polarization indicates that the average diameter of the beam in the waist region decreases with increasing frequency and ranges from 2.3 mm to 1.5 mm in the frequency range of 0.2–1 THz. The asymmetry of the beam in the (x, y) plane depends on the frequency and does not exceed 10%.

To improve the quality of the recorded terahertz image due to effects associated with the formation of highly localized regions (terajets), a polytetrafluoroethylene (PTFE) sphere with a diameter of $d \sim 2.3$ mm was placed immediately near the surface of the sample (see Figs. 1d and 1e). In our experiments, the spherical shape of a focusing particle was chosen due to the simplicity of its fabrication. The geometry and surface quality of the spherical particle were controlled using optical methods (an Olympus BX 43 optical microscope equipped with 100× and 5× objectives). We neglected the effects caused by the additional scattering of terahertz radiation due to surface roughness, as the measured surface roughness was no more than 15–30 μm [26]. The accurate positioning of the dielectric sphere with respect to the surface of the sample and to the center of the waist of the focusing parabolic mirrors was performed using a three-coordinate linear translator (see Fig. 1c) equipped with micrometer screws (the minimum displacement step was 10 μm). A 632-nm laser was used to accurately localize the sphere in the center of an iris diaphragm (maximum aperture of 15 mm) used as a sample holder (see Figs. 1e and 1f).

In our experiments, the terahertz pulse propagated through the dielectric sphere immediately before the interaction with the sample. The signal transmitted through the system was detected in the far-field region (the distance from the sphere to the detector is $r \gg \lambda$) [27].

To quantitatively estimate the effect of the additional focusing particle on the spatial resolution of the scanning system, we used a test sample consisting of alternating transparent and opaque converging circular sections (see Fig. 2a, the outer diameter is 3 mm) deposited on a 0.5-mm-thick SiO_2 plate by photolithography (MLA100, Heidelberg Instruments Mikotechnik, Germany). This pattern, commonly known as the Siemens star [28], is widely used to estimate the spatial resolution of optical systems in a wide frequency range [29–31].

RESULTS AND DISCUSSION

Figure 2 presents terahertz images of the metallic structure on the SiO_2 substrate obtained (b) without and (c, d) with the PTFE sphere in the beam. It is seen that the dielectric particle significantly improves the spatial resolution of the system as a whole. The standard approach to estimate the resolution using the selected test sample involves analyzing the in the central part of the image (see Fig. 2c). The spatial resolution of the system significantly depends on the frequency of the incident electromagnetic radiation. The black line in Fig. 2e is the experimentally evaluated frequency dependence of the spatial resolution of the terahertz spectrometer matched to the PTFE sphere as the focusing particle. The analysis of this dependence shows that the minimum resolution corresponds to a frequency of 0.5 THz and was about 0.38λ, which is close to the theoretical limit 0.33λ [20].

As mentioned above, the position of the dielectric sphere with respect to the center of the waist of the terahertz beam is an important practical factor that affects the main characteristics of the terajet and, consequently, the quality of the resulting image. In this work, to simulate the scattering of the electromagnetic wave on the spherical particle, we used the model of the linearly polarized Gaussian beam whose electric field in the paraxial approximation can be represented in the form

$$E = A\frac{w_0^2}{w_0^2 + 2iz/k_0}\exp\left(ik_0 z - \frac{\rho^2}{w_0^2 + 2iz/k_0}\right). \quad (1)$$

Here, ρ is the polar coordinate in the cross section of the beam; z is the longitudinal coordinate; A is the field at the point $(\rho = 0, z = 0)$; $k_0 = 2\pi f/c$ is the wave vector in vacuum, where f is the frequency and c is the speed of light in vacuum; and w_0 is the waist radius of the Gaussian beam.

We considered the scattering of a terahertz wave whose electric field is given by Eq. (1) on the dielectric sphere. The origin of the Cartesian coordinate system was chosen in the center of the sphere. The scattered field was calculated using the so-called operator theory, which was first proposed in [32] and was successfully applied to study optical forces acting on homogeneous [33] and inhomogeneous particles [34]. This theory is based on the symmetry of the scattering object, which allows Maxwell's equations to be reduced to the system of ordinary differential equations for the corresponding electric and magnetic fields whose fundamental solution can be represented in the form of the product of the evolution operator (four-dimensional matrix) and the four-dimensional tangential field vector at the initial point. The application of boundary conditions allows the calculation of the scattered field amplitude vector. It is noteworthy that the considered approach is applicable for an arbitrary incident field.

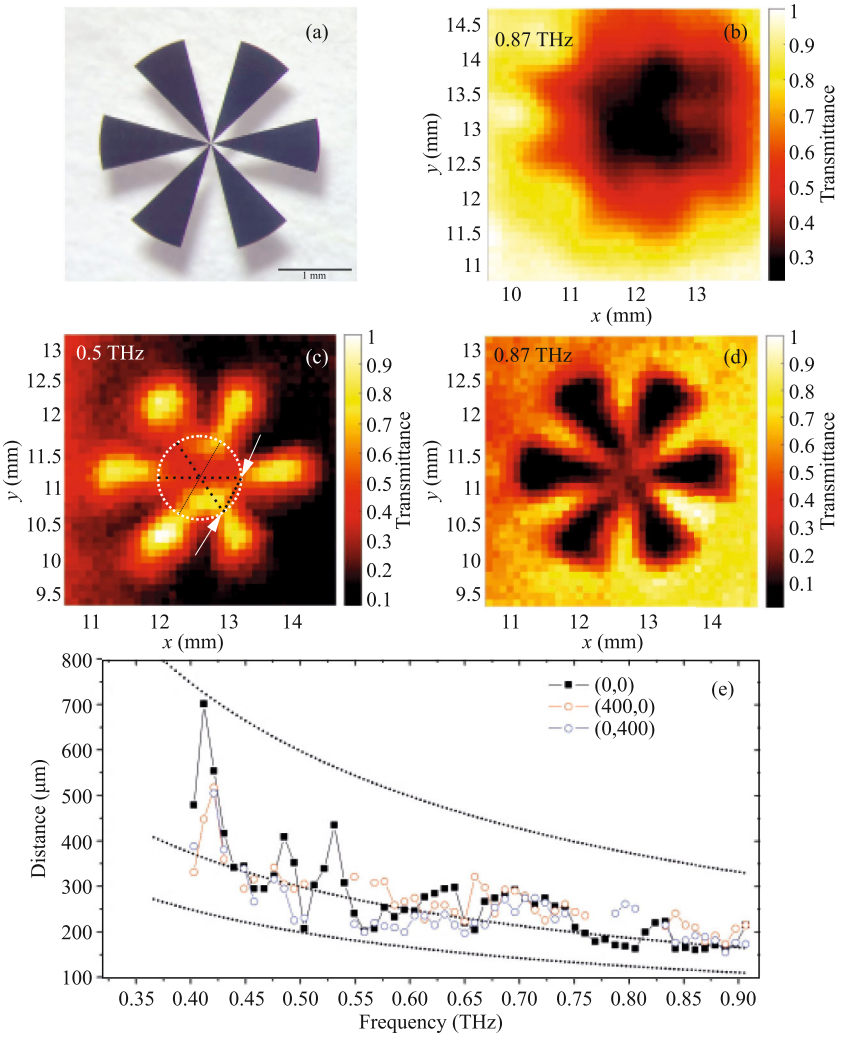

Fig. 2. (Color online) (a) Optical image of the test SiO_2 plate sample with a metallic structure on the surface (Siemens star). (b, d) Terahertz images of the test structure at a frequency of 0.87 THz (b) without and (d) with the dielectric sphere in the beam. (c) Terahertz image of the test structure with the dielectric sphere at a frequency 0.5 THz. The dimensions of the images are 4×4 mm^2. Scanning step along the x and y axes was 102 μm, and the distance between the surface of the sphere and the sample was 200 μm. (e) Frequency dependence of the chord length of the minimal circle plotted in the central part of images of the test structure.

Figure 3 presents the field distribution near the surface of the dielectric sphere exposed to the radiation with the frequency $f = 0.7$ THz. In our simulations, we used parameters that closely matched the experimental conditions: the waist radius of the terahertz Gaussian beam was $w_0 = 1.1$ mm; the diameter and refractive index of the sphere were $d = 2.3$ mm and $n = 1.47$, respectively; and the refractive index of the environment was 1. The incident terahertz pulse propagated in the positive z direction. The calculations were performed for x- and y-polarized radiation. It is seen in Figs. 3a–3f that the region of a high intensity $I \sim |E|^2$, i.e., terajet, is formed immediately behind the sphere irradiated by the Gaussian beam whose diameter is comparable to the diameter of the sphere ($2w_0 = d$). The FWHM of the jet at the focus for the x- and y-polarized wave is 0.70λ and 0.56λ, respectively. It is worth noting that the achievement of the minimum-diameter terajet is beyond the scope of this study and our focus is solely to demonstrate the primary features of the images obtained using such localized fields. The analysis of the intensity distribution in the (x, y) plane, perpendicular to the beam propagation direction immediately near the surface of the sphere ($z = 1.15$ mm, the case $\delta z = 0$ in Fig. 3g), clearly demonstrates the asymmetry of the terajet with respect to the polarization of the incident radiation [36]. It is worth noting that this asymmetry becomes less pronounced when the (x, y) plane is shifted along the z axis (see Fig. 3g, the case $\delta z = 200$ μm).

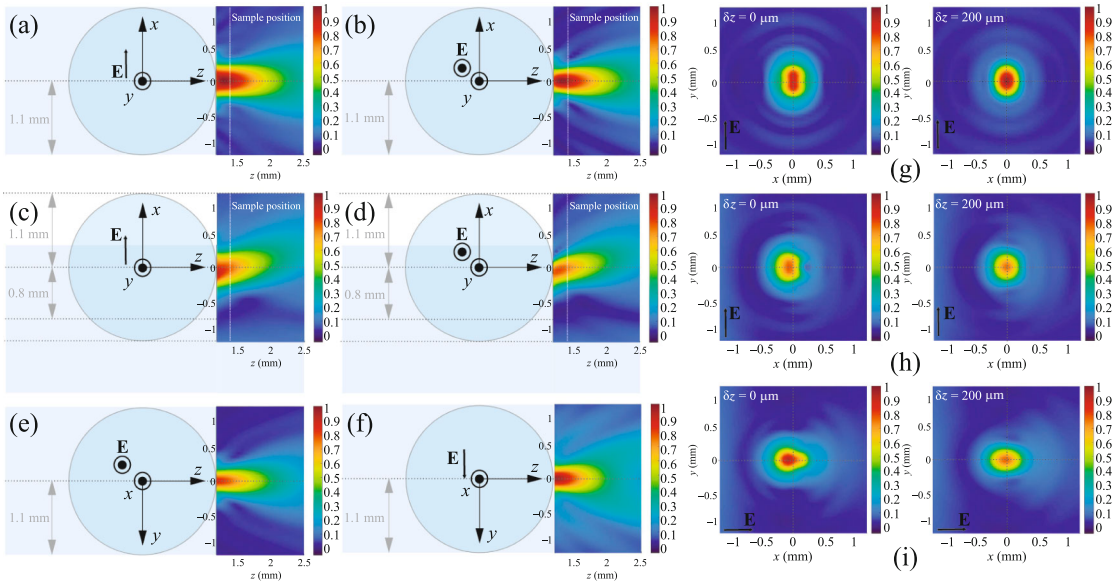

Fig. 3. (Color online) Distribution of the scattered field amplitude $|E|$ in arbitrary units near the surface of the dielectric sphere calculated at a frequency of 0.7 THz for (a, b) the dielectric sphere placed in the center of the terahertz beam and (c–f) the dielectric sphere shifted by 800 μm (~0.34d) along the x axis. Scattered field distribution in the (x, y) plane perpendicular to the propagation direction of the incident electromagnetic wave at $\delta z = 0$ and 200 μm for the dielectric sphere (g) placed in the center of the terahertz beam and (h, i) shifted by 800 μm along the x axis. All calculations were performed for two orthogonal polarization direction of the incident electromagnetic wave. The discretization step along the vertical and horizontal axes was 54 μm.

When the sphere was shifted from the waist center by δ_{sphere}, its surface was illuminated incompletely (the violating the axial symmetry of the system, which leads to the bending of the field localization region and to the formation of the photonic hook [37]. Figures 3c–3f present the field distribution of the incident terahertz radiation with x and y linear polarizations. The sphere was shifted in the x direction by $\delta_{sphere} = 800$ μm (~0.34d) in both cases. It is noteworthy that all distributions in Fig. 3 are normalized to the maximum calculated amplitude of the scattered field for the sphere in the center of the beam $\delta_{sphere} = 0$. The presented distributions demonstrate two key points. First, the shift of the sphere results in the bending of the terajet towards the center of the particle, which is equivalent to the corresponding shift of the terahertz beam and should be manifested in the experiment as the shift of the recorded image. Second, the maximum intensity in the focus of the photonic hook for the system with the shifted sphere decreases.

In [38], we have already demonstrated that the photonic hook can be generated using a metal mask screening a part of the wavefront of the electromagnetic wave incident on a dielectric cylinder. Such an additional screen in the system leads to the re-reflection of radiation and the redistribution of the scattered field both inside the dielectric particle and near its surface, which can enhance the field in the focus of the photonic hook under certain conditions. However, as shown in this work (data are not presented), such an approach significantly worsens the quality of images recorded at certain frequencies.

According to the profile of the photonic hook in the (x, y) plane (see Figs. 3h and 3i), the shift δ_{sphere} perpendicular to the polarization direction E (y-polarized wave in Fig. 3h) leads to the broadening of the beam, which should affect the resolution of the scanning system as a whole. The shift of the sphere in the polarization direction ($\delta_{sphere} \parallel E$, x-polarized wave in Fig. 3i) hardly results in the broadening of the beam. Regardless of the polarization of the incident terahertz radiation, the shift of the particle leads to the focus of the scattered field in the z axis towards the surface of the sphere and, as a result, to a decrease in the focusing depth of the system as a whole (see Fig. 3).

To demonstrate the effects discussed above, Figs. 4b and 4c present the experimentally recorded images of the Siemens star for the shift $\delta_{sphere} = 800$ μm of the PTFE sphere in the y and x directions parallel and perpendicular to the polarization of the incident beam, respectively. It is seen that the shift of the dielectric sphere leads to the shift of the image, which qualitatively agrees with the numerical calculations and thus provides experimental evidence of the formation of the photonic hook near the surface of the sphere. Figure 4d shows the dependences of the shift

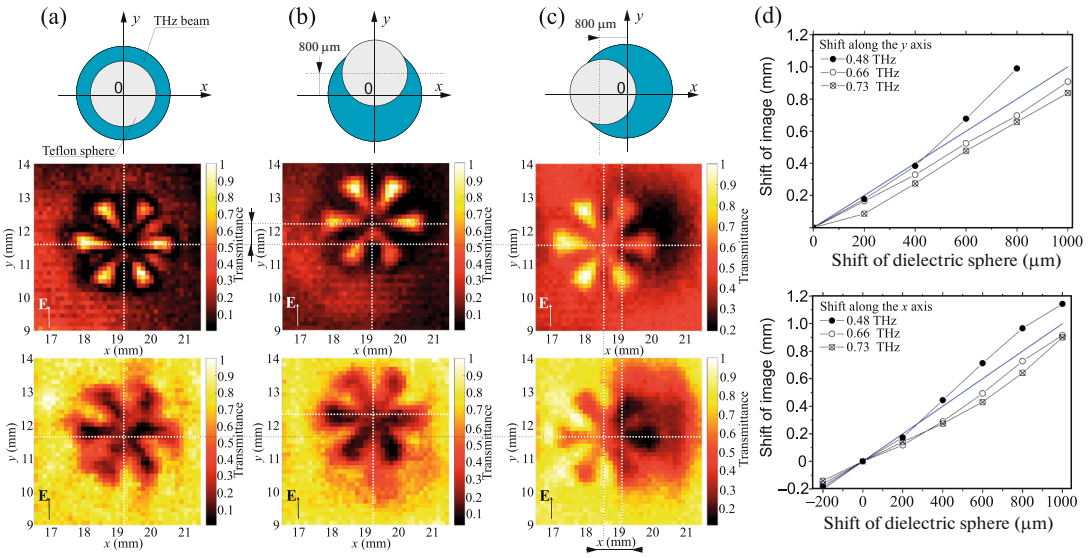

Fig. 4. (Color online) Images of the Siemens star on the SiO_2 substrate obtained using the PTFE sphere 2.3 mm in diameter placed in the terahertz beam for (a) the dielectric sphere placed in the center of the waist of the terahertz Gaussian beam and (b, c) the dielectric sphere shifted by 800 μm (0.35*d*) along the (b) *y* and (c) *x* axes with respect to the center of the waist of the terahertz Gaussian beam. The dimensions of the images are 4 × 4 mm. Scanning step along the *x* and *y* axes was 102 μm, and the distance between the surface of the sphere and the sample was 200 μm. (d) Shift of the center of the Siemens star δ_{image} versus the shift of the PTFE sphere δ_{sphere} at three frequencies when the shift of the sphere δ_{sphere} is (upper part) parallel and (lower part) perpendicular to the electric field polarization *E*. The blue line is the linear dependence $\delta_{image} = \delta_{sphere}$.

δ_{image} of the image of the center of the Siemens star in two perpendicular directions on the shift of the sphere δ_{sphere}. The analysis of these dependences indicates that the shift of the sphere results in the proportional shift of the image $\delta_{image} \sim b\delta_{sphere}$, where $b \neq 1$ in the general case. The coefficient *b* should obviously depend both on the position of the sample with respect to the sphere ($\delta z > d$) and on the frequency of the incident radiation *f*. The latter is due to the frequency dependence of the focus position of the photonic jet (see [22, 24]).

The asymmetry of the image of the Siemens star along the *y* axis, which is clearly seen in the central region of the structure, aligns well with the total asymmetry of the photonic hook considered above (see Fig. 3) and can be used as a criterion of the location of the test sample near the focus of such a dielectric lens. The measured frequency dependences of the spatial resolution for the cases of the shift $\delta_{sphere} = 400$ μm of the sphere along the *x* and *y* axes are presented in Fig. 2e by the red and blue lines, respectively. They show that this shift of the focusing particles hardly worsens the resolution of the scanning system as a whole. However, one can observe that additional artifacts appear at $\delta_{sphere} > 400$ μm (~0.17*d*) (see Figs. 4d and 4c), and their presence significantly reduces the imaging contrast at certain frequencies.

Figures 5a–5d present images of the test structure recorded at frequency of 0.8 THz and with shifts δ_{sphere} = (a) 0, (b) 200, (c) 600, and (d) 800 μm of the PTFE sphere from the waist center of the terahertz Gaussian beam along the *x* axis. The corresponding numerically calculated field distributions are shown in Figs. 5e and 5f, where an additional low-intensity beam propagating symmetrically with respect to the center of the incident radiation (in our notation, the waist center has the coordinate $x = -0.8$ mm and is marked by the vertical dotted straight line in Fig. 5f) is observed. This additional beam is due to the interference of the scattered field and the part of the wavefront of the incident terahertz wave that is not covered by the particle. One can see that the experimental data presented in Fig. 5, collected using the near-field enhancement technique with additional system asymmetry due to sphere displacement, are in good agreement with our numerical calculations. Vertical dotted straight lines in Figs. 5a–5d correspond to the center of the initial Gaussian beam, and two images are mirror symmetric with respect to these lines.

CONCLUSIONS

This work continues the previous studies of the practical possibility of using terajets to achieve a subwavelength resolution in existing terahertz systems. In particular, it has been shown that the displacement of the focusing spherical particle from the center of the

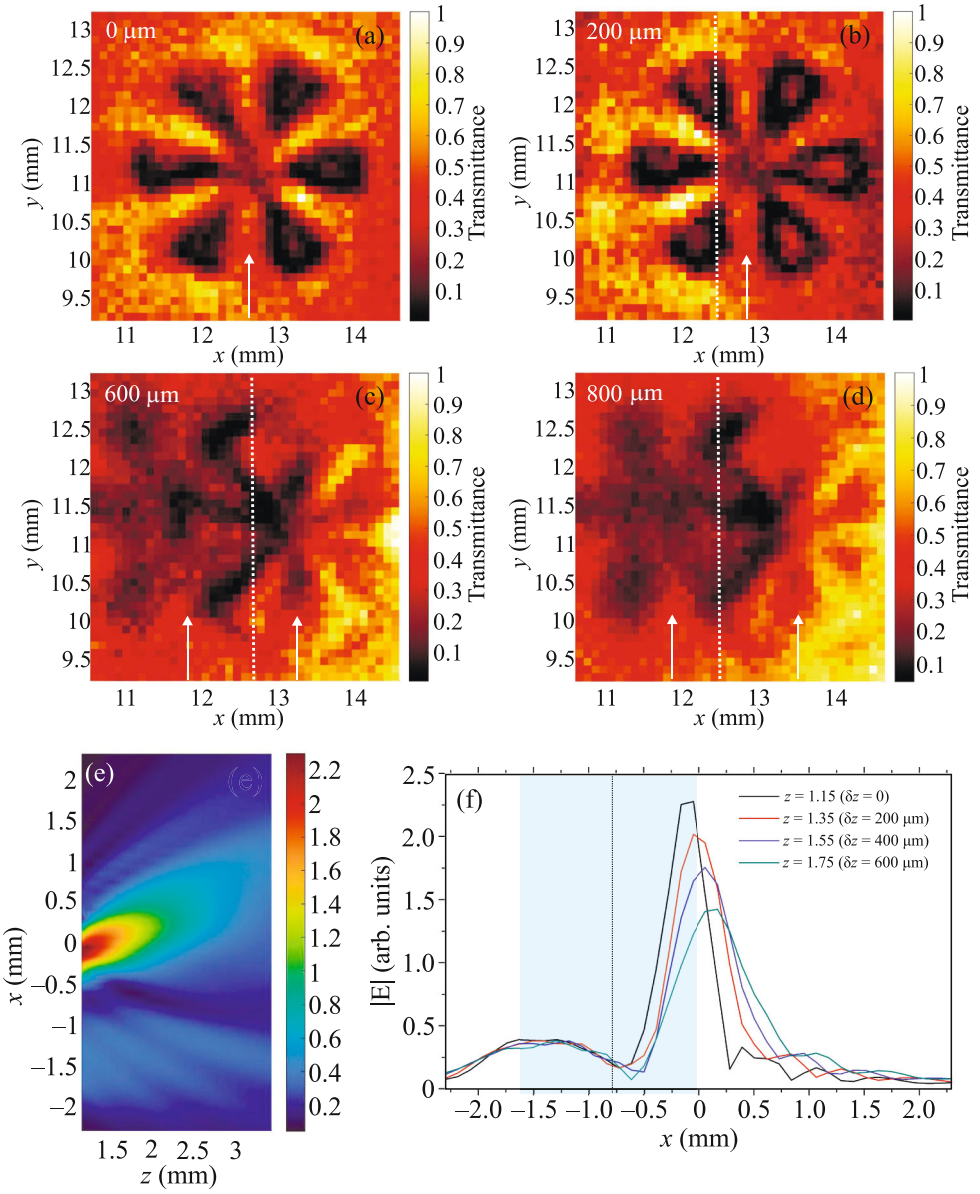

Fig. 5. (Color online) Images of the Siemens star at a frequency of 0.8 THz for the shifts δ_{sphere} = (a) 0, (b) 200, (c) 600, and (d) 800 μm along the x axis from the center of the waist of the terahertz Gaussian beam. The distance between the surface of the sphere and the sample was 200 μm. The dimensions of the images are 4 × 4 mm. Arrows mark images obtained using the terajet and the beam part nonoverlapped by the spherical particle. (e) Distribution of the scattered field amplitude near the surface of the dielectric sphere calculated at a frequency of 0.8 THz. (f) Electric field distributions along the x axis at several z values. The calculations were carried out with the diameter of the sphere $d = 2.3$ mm, the waist diameter of the Gaussian beam $2w_0 = 1.5$ mm, the shift of the sphere $\delta_{sphere} = 800$ μm, the y-polarization of the field, and the discretization steps 120 and 56 μm along the horizontal and vertical axes, respectively.

Gaussian beam in the plane perpendicular to its propagation direction results in the bending of the terajet and in the formation of the photonic hook, which is subsequently manifested in experimentally recorded terahertz images. It is worth noting that the shift of the image in the general case depends on the frequency. The frequency dependences of the spatial resolution indicate that the bending of the spatial shape of the terajet hardly worsens the recorded images. However, the existing extreme bending value determined by the ratio of the diameter of the terahertz beam to the size of the focusing particle limits the possibility of hyperspectral scanning using such a system because the appearance of additional artifacts. Thus, it has been experimentally demonstrated that, being relatively simple to implement, the presented technique allows

for a significant increase in the resolution of commercial terahertz scanning systems, thereby extending their application domain.

FUNDING

This work was supported by program of excellence for the National Research Tomsk Polytechnic University and by the Belarusian Republican Foundation for Basic Research (project no. F23ME-023). A.V. Novitsky acknowledges the support of the Research Program "Convergence-2025" (project no. 2.1.02.1).

CONFLICT OF INTEREST

The authors of this work declares that they have no conflicts of interest.

OPEN ACCESS

REFERENCES

1. A. Glagolewa-Arkadiewa, Nature (London, U.K.) **113**, 640 (1924).
2. Y. H. Tao, A. J. Fitzgerald, and V. P. Wallace, Sensors **20**, 1424 (2020).
3. A. Leitenstorfer, A. S. Moskalenko, T. Kampfrath, et al., J. Phys. D: Appl. Phys. **56**, 223001 (2023).
4. Y. Huang, Y. Shen, and J. Wang, Engineering **22**, 106 (2023).
5. K. Yamada, Y. Samura, O. V. Minin, A. Kanno, N. Sekine, J. Nakajima, I. V. Minin, and S. Hisatake, Front. Commun. Networks **2**, 2673 (2021).
6. N. V. Chernomyrdin, A. O. Shchadko, S. P. Lebedev, I. E. Spektor, V. L. Tolstoguzov, A. S. Kucheryavenko, K. M. Malakhov, G. A. Komandin, V. S. Gorelik, and K. I. Zaytsev, Opt. Spectrosc. **124**, 428 (2018).
7. T. R. Globus, D. L. Woolard, T. Khromova, T. W. Crowe, M. Bykhovskaia, B. L. Gelmont, J. Hesler, and A. C. Samuels, J. Biol. Phys. **29**, 89 (2003).
8. Y. Huang, X. Yang, and J. Li, J. Appl. Polym. Sci. **140**, e54737 (2023).
9. P. Kuzel and H. Nemec, Adv. Opt. Mater. **8**, 1900623 (2020).
10. O. V. Minin and I. V. Minin, Quantum Electron. **52**, 13 (2022).
11. N. Chopra and J. Lloyd-Hughes, J. Infrar. Millim. Terahertz Waves **44**, 981 (2023).
12. C. Bruckner, G. Notni, and A. Tunnermann, Optik **121**, 113 (2010).
13. Y. H. Lo and R. Leonhardt, Opt. Express **16**, 15991 (2008).
14. A. Pimenov and A. Loidl, Appl. Phys. Lett. **83**, 4122 (2003).
15. D.-H. Choi, J.-H. Shin, I.-M. Lee, and K. H. Park, Sensors **21**, 1424 (2021).
16. D.-H. Choi, M. Kim, D. W. Park, E. S. Lee, and I.-M. Lee, Opt. Laser Technol. **174**, 110557 (2024).
17. H. H. Nguyen Pham, S. Hisatake, O. V. Minin, T. Nagatsuma, and I. V. Minin, APL Photon. **2**, 056106 (2017).
18. V. Pacheco-Peña, M. Beruete, I. V. Minin, and O. V. Minin, Appl. Phys. Lett. **105**, 084102 (2014).
19. A. Mandal and V. R. Dantham, J. Opt. Soc. Am. B **37**, 977 (2020).
20. A. Heifetz, S.-C. Kong, A. V. Sahakian, A. Taflove, and V. Backman, J. Comput. Theor. Nanosci. **6**, 1979 (2009).
21. A. Mandal, P. Tiwari, P. K. Upputuri, and V. R. Dantham, Sci. Rep. **12**, 173 (2022).
22. L. Yue, Z. Wang, B. Yan, J. N. Monks, Y. Joya, R. Dhama, O. V. Minin, and I. V. Minin, Ann. Phys. **532**, 2000373 (2020).
23. A. L. S. Cruz, C. M. B. Cordeiro, and M. A. R. Franco, Proc. SPIE **9634**, 963412 (2015).
24. A. G. Paddubskaya, N. I. Valynets, A. V. Novitsky, I. V. Minin, and O. V. Minin, J. Phys. D: Appl. Phys. **57**, 145104 (2024).
25. S. Hunsche, M. Koch, I. Brener, and M. C. Nuss, Opt. Commun. **150**, 22 (1998).
26. R. Chen, J. Lin, P. Jin, M. Cada, and Y. Ma, in *Proceedings of the 2015 IEEE 28th Canadian Conference on Electrical and Computer Engineering (CCECE), Halifax, NS, Canada* (2015), p. 1393. https://doi.org/10.1109/CCECE.2015.7129483
27. M. Kerker, *The Scattering of Light and Other Electromagnetic Radiation* (Wiley, New York, 1969).
28. A. Orych, Int. Archives Photogramm. Remote Sens. Spatial Inform. Sci. **XL-1/W 4**, 391 (2015).
29. R. I. Stantchev, B. Sun, S. M. Hornett, P. A. Hobson, G. M. Gibson, M. J. Padgett, and E. Hendry, Sci. Adv. **2**, e1600190 (2016).

30. R. I. Stantchev, D. B. Phillips, P. Hobson, S. M. Hornett, M. J. Padgett, and E. Hendry, Optica **4**, 989 (2017).
31. S.-C. Chen, L.-H. Du, K. Meng, J. Li, Z.-H. Zhai, Q.-W. Shi, Z.-R. Li, and L.-G. Zhu, Opt. Lett. **44**, 21 (2019).
32. A. Novitsky and L. Barkovsky, Phys. Rev. A **77**, 033849 (2008).
33. A. Novitsky, C.-W. Qiu, and H. Wang, Phys. Rev. Lett. **107**, 203601 (2011).
34. A. Novitsky, A. S. Shalin, and A. V. Lavrinenko, Phys. Rev. A **95**, 053818 (2017).
35. F. D'Angelo, Z. Mics, M. Bonn, and D. Turchinovich, Opt. Express **22**, 12475 (2014).
36. T. Uenohara, Y. Mizutani, and Y. Takaya, Precis. Eng. **60**, 274 (2019).
37. O. V. Minin and I. V. Minin, *The Photonic Hook: From Optics to Acoustics and Plasmonics* (Springer, Cham, Switzerland, 2021).
38. I. V. Minin, O. V. Minin, C.-Y. Liu, H.-D. Wei, Y. E. Geints, and O. Karachevsky, Opt. Lett. **45**, 4899 (2020).